Ultrasonics 97 (2019) 57–62

Contents lists available at ScienceDirect

Ultrasonics

journal homepage: www.elsevier.com/locate/ultras

Non-paraxial multi-Gaussian beam model of Leaky Rayleigh waves generated by a focused immersion transducer

Shan Li[a], Joseph A. Turner[b], Lester W. Schmerr[c], Xiongbing Li[a,*]

[a] School of Traffic and Transportation Engineering, Central South University, Changsha, Hunan 410075, China
[b] Mechanical and Materials Engineering, University of Nebraska-Lincoln, Lincoln, NE 68588, USA
[c] Center for NDE, Iowa State University, Ames, IA 50011, USA

ARTICLE INFO

Keywords:
Leaky Rayleigh wave
Non-paraxial Multi-Gaussian beam model
Focused immersion transducer
Attenuation coefficient

ABSTRACT

A non-paraxial multi-Gaussian beam (NMGB) model is proposed for Leaky Rayleigh Waves (LRWs) generated by a focused immersion transducer at oblique incidence. Using the NMGB model, the velocity fields are calculated and compared with the corresponding results obtained by the paraxial multi-Gaussian beam (MGB) model and the more exact Rayleigh–Sommerfeld integral (RSI) model. Numerical results show that the LRW beam behavior obtained using the NMGB model agrees well with that using the RSI model, but the NMGB model is much more efficient. Moreover the NMGB model overcomes the accuracy limitation of the MGB model. Good agreement between the NMGB model and experimental measurements for both on-axis and off-axis fields is obtained when an attenuation coefficient is introduced. In addition, this model can be used to measure the attenuation coefficient with consideration of the diffraction attenuation. It is observed that the attenuation coefficient of the LRW will increase when the acoustic impendence differences between the solid and fluid decrease. The NMGB model described in this article provides an efficient tool for calculating the velocity fields of the LRW and is therefore significant for practical applications of ultrasonic measurements.

1. Introduction

Leaky Rayleigh waves (LRWs), propagating at a fluid/solid interface, are sensitive to surface and near-surface flaws in solids [1,2]. The LRW can be generated in an immersion test system when longitudinal waves impinge obliquely upon the fluid/solid interface [2]. LRWs have a highly concentrated sound beam and energy [3], and are widely used to detect flaws in the structure [4] and evaluate material properties in many applications [5–7]. Accurate models of the LRW velocity field are important for analyzing the detection capabilities of a system [8], optimizing an ultrasonic experimental configuration [9], and quantitatively evaluating the detected flaws [10]. Highly accurate and efficient models of the LRW can have a significant impact on nondestructive detection evaluation (NDE) of materials and components [11,12].

Current methods to calculate the velocity field for Rayleigh waves include the Rayleigh–Sommerfeld integral (RSI) model [11,13], the multi-Gaussian beam (MGB) model [14–19] and the distributed point source method (DPSM) [20–22]. The velocity fields for Rayleigh waves have been built with the RSI model and the MGB model, respectively. Schmerr et al. [11] used the superposition of Green's functions and the stationary phase approximation to develop an RSI model for calculating the Rayleigh wave velocity fields generated by angle beam wedge transducers. Zhao et al. [18,19] introduced the MGB model to simplify the calculation process and increase computational efficiency. These researchers have established the basis for modeling the LRW velocity fields in an immersion testing setting. However, the MGB model proposed by Zhao et al. is based on the paraxial approximation, and is not accurate for side lobes, and these models are focused on the Rayleigh waves generated by a planar transducer. Banerjee and Kundu used the DPSM to calculate ultrasonic fields in solids immersed in a fluid for detection of internal anomalies [22]. Although this method does not require any far-field approximation, and can avoid the accuracy problem of the paraxial approximation, it is only a semi-analytical resolution. We expect to give a clear analytical solution, which can be introduced to the ultrasonic measurement model [11,23] and the diffuse backscatter model [24,25] in the future, in which we can evaluate the flaw size and the grain size near surface later.

In addition, the leaky attenuation is not taken into account in all above methods and it is an important aspect of LRW propagation. Attenuation is the result of continuous radiation (i.e. leaking) back into the fluid [4], and has a great effect on the velocity field of the LRW. Due to the presence of amplitude loss caused by diffraction, it is difficult to

* Corresponding author.
E-mail address: lixb_ex@163.com (X. Li).

https://doi.org/10.1016/j.ultras.2019.04.006
Received 28 January 2019; Received in revised form 24 April 2019; Accepted 29 April 2019
Available online 30 April 2019
0041-624X/

isolate the effect of the leakage attenuation. To address prior limitations, a non-paraxial multi-Gaussian beam (NMGB) model is developed in this article to calculate the beam fields generated by a focused transducer. Thus, the main purpose of this article is to model the LRW velocity fields generated by a focused immersion transducer theoretically and investigate their characteristics experimentally. First, the generation process of the LRW is briefly illustrated and the RSI model, the NMGB model and the MGB model for the LRW velocity fields are derived. Then, the results of different models are provided, and effects of water path and transducer parameters on the beam behavior are discussed. The LRW velocity fields at the water/steel and water/aluminum interfaces are measured to verify the proposed theoretical models and study the LRW velocity field behavior. Finally, the attenuation coefficients of the LRW for water/aluminum and water/steel interfaces are measured and discussed with consideration of the diffraction attenuation.

2. Theory

2.1. Leaky Rayleigh wave generation

The generation of the LRW and the coordinate system used are shown in Fig. 1. When an immersion transducer is placed at an oblique incidence angle ψ greater than the critical angle θ, the mode-converted LRWs can be generated [3]. These waves propagate along the solid surface with a penetration depth of about one wavelength and leak energy into the fluid [26]. The origin of the (x_1, y_1, z_1) coordinates is in the center of the transducer and that of (x_2, y_2, z_2) is located at the intersection of the transducer center axis and the specimen surface. The coordinates z_1 and z_2 are taken normal to the transducer and the plane surface of the sample, respectively.

The incident angle can be calculated using Snell's law, and is related to the velocity c of the wave along the fluid-solid interface. This velocity satisfies the following generalized Rayleigh equation [27]

$$4\left(\frac{c_p}{c}\right)^2\left[1-\left(\frac{c_p}{c}\right)^2\right]^{1/2}\left[\left(\frac{c_p}{c_s}\right)^2-\left(\frac{c_p}{c}\right)^2\right]^{1/2}+\left[1-2\left(\frac{c_p}{c}\right)^2\right]^2 = -i\frac{\rho_f}{\rho_s}\left[\frac{(c_p/c)^2-(c_p/c_s)^2}{(c_p/c_f)^2-(c_p/c)^2}\right], \tag{1}$$

with

$$c_r = 1/Re(1/c), \quad \sin\theta = c_f/c_r, \tag{2}$$

where Re indicates the "real part". c_f is the longitudinal wave velocity of fluid. c_p and c_s are the longitudinal and shear wave velocities of the solid, respectively. c_r is the LRW velocity. ρ_f and ρ_s are the densities of the fluid and sample, respectively. θ is the critical angle.

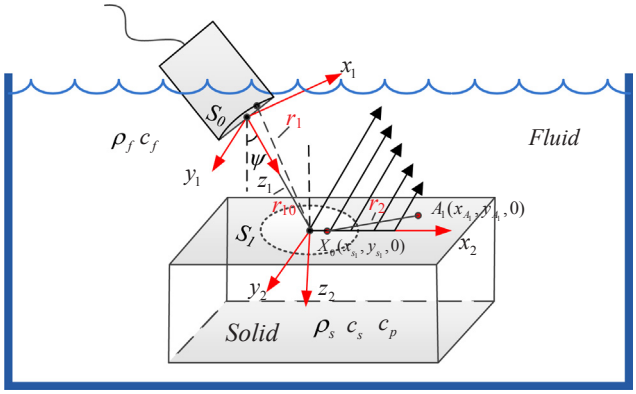

Fig. 1. Schematic diagram of the LRW generation and the definition of the coordinate systems.

2.2. Rayleigh-Sommerfeld integral model of the LRW

The case of a focused immersion transducer radiating the LRW along the surface of the sample is considered using the Rayleigh-Sommerfeld integral (RSI). The velocity field of the LRW $v(x_{A_1}, y_{A_1})$ can be written as [28]

$$v(x_{A_1}, y_{A_1}) = \frac{-i\omega T}{4Qc_r}\frac{\exp(i\pi/4)}{\sqrt{2\pi k_r}} \times \int_{S_1} p(x_{s_1}, y_{s_1}, \omega)G(x_{A_1}, y_{A_1}, x_{s_1}, y_{s_1})dS_1(x_{s_1}, y_{s_1}), \tag{3}$$

with

$$G(x_{A_1}, y_{A_1}, x_{s_1}, y_{s_1}) = \exp(ik_r r_2)/\sqrt{r_2}, \tag{4}$$

and

$$T = \frac{\rho_f c_f}{\rho_s c_r}\left(T^{p,p}\frac{c_s}{c_p}\left(\frac{c_p^2}{c_s^2}-2\frac{c_p^2}{c_r^2}\right)-2iT^{s,p}\frac{c_s}{c_r}\sqrt{\frac{c_s^2}{c_r^2}-1}\right), \tag{5}$$

where $T^{p,p}$ and $T^{s,p}$ are the ordinary plane wave transmission coefficients for longitudinal waves and shear waves, for a fluid/solid in smooth contact [28]. Q defines the "power flow" which is given in [19]. ω is the circular frequency and $k_r = \omega/c_r$ is the wave number of the LRW in the sample. The parameter $r_2 = \sqrt{(x_{A_1}-x_{s_1})^2+(y_{A_1}-y_{s_1})^2}$ defines the distance from any point $X_0(x_{s_1}, y_{s_1}, 0)$ of the source area S_1, to an arbitrary point $A_1(x_{A_1}, y_{A_1}, 0)$ on the surface of the solid. $p(x_{s_1}, y_{s_1}, \omega)$ is the pressure field (sound source of the LRW) on the surface of the sample radiated from the focused transducer. It can be expressed using a modified Rayleigh-Sommerfeld integral as [11]

$$p(x_{s_1}, y_{s_1}, \omega) = \frac{-i\omega\rho_f}{2\pi}v(x_{s_0}, y_{s_0}, \omega) \times \int_{S_0}\exp\left(\frac{-ik_f l^2}{2F}\right)\frac{\exp(ik_f r_1-\alpha_f r_1)}{r_1}dS_0(x_{s_0}, y_{s_0}), \tag{6}$$

where $l = \sqrt{x_{s_0}^2+y_{s_0}^2}$, $k_f = \omega/c_f$ is the wave number in fluid, and F is the focal length of the transducer. α_f is the attenuation coefficient for longitudinal waves in the fluid and the parameter $r_1 = \sqrt{(x-x_{s_0})^2+(y-y_{s_0})^2+z^2}$ defines the distance from an arbitrary point on the sample surface to arbitrary point on the transducer surface, S_0.

Placing Eq. (5) into Eq. (3), the velocity field of the LRW can be expressed as

$$v(x_{A_1}, y_{A_1}) = \frac{-T\omega\rho_f k_r}{8\pi Q}\frac{\exp(i\pi/4)}{\sqrt{2\pi k_r}}v_0(x_{s_0}, y_{s_0}, \omega) \times \int_{S_1}\int_{S_0}\exp\left(\frac{-ik_f l^2}{2F}\right)\frac{\exp(ik_f r_1-\alpha_f r_1)}{r_1}\frac{\exp(ik_r r_2-\alpha_{LRW} r_2)}{\sqrt{r_2}}dS_0 dS_1, \tag{7}$$

where α_{LRW} is the attenuation coefficient of the LRW to account for losses as the wave propagates along the surface of the sample. The velocity $v_0(\omega)$ at the transducer face is assumed to be uniformly distributed and the initial value is set as unit. The RSI model is commonly used by numerical solution of the integral in Eq. (7). Note that, when $A_1(x_{A_1}, y_{A_1}, 0)$ is outside S_1 area, the hole S_1 area is used for the integration, and when $A_1(x_{A_1}, y_{A_1}, 0)$ is located in S_1 area, the integral area is changed. For more details, see Ref. [29].

2.3. Multi-Gaussian beam model of the LRW

Although the RSI can be used to calculate the radiation beam field from focused transducers exactly, it requires a large computation cost. Thus, a general MGB model is often used to simplify the computations. In this case, we assume that $k_f a \gg 1$, where a is the radius of the transducer, such that the beam is reasonably directional and localized in the vicinity of the x_2 axis. First, the uniform normal velocity on the transducer surface is expanded as a superposition of several Gaussian beams [14]. For a focused transducer, the velocity over the transducer face can be expressed as [15]

$$v(x_{s_0}, y_{s_0}, \omega)\exp\left(\frac{-ik_f l^2}{2F}\right) = \sum_{n=1}^{25} A_n \exp(-B_n(x_{s_0}^2 + y_{s_0}^2)/a^2), \tag{8}$$

with

$$B_n \to B_n + ik_f a^2/(2F), \tag{9}$$

where A_n, B_n are 25 groups of complex coefficients that reproduce accurately the velocity field of an immersion transducer [11]. Using the paraxial approximation, the factor $\exp(ik_f r_1)/r_1$ can be simplified as [18]

$$\frac{\exp(ik_f r_1)}{r_1} \approx \frac{1}{z}\exp[ik_f(z + (x - x_{s_0})^2/2z + (y - y_{s_0})^2/2z)]. \tag{10}$$

The Green's function of Eq. (4) can be approximated as [19]

$$G(x_{A_1}, y_{A_1}, x_{s_1}, y_{s_1}) = \frac{\exp(ik_r r_2)}{\sqrt{r_2}} \approx \frac{1}{\sqrt{x_{A_1}}}\exp\left[ik_r\left(x_{A_1} + \frac{y_{A_1}^2}{2x_{A_1}} + \frac{y_{s1}^2}{2x_{A_1}} - x_{s_1} - \frac{y_{A_1}y_{s1}}{x_{A_1}}\right)\right]. \tag{11}$$

Placing Eqs. (8)–(11) into Eq. (7), an expression for the MGB model calculated by the paraxial approximation can be obtained as

$$v(x_{A_1}, y_{A_1}) = \frac{T\omega\rho_f\pi}{2Q}\frac{\exp(i\pi/4)}{\sqrt{2\pi k_r}}\sum_{n=1}^{25}\frac{A_n}{1 + iB_n r_{10}/D} \times \frac{\exp(ik_f r_{10} + ik_r x_{A_1} - \alpha_f r_{10} - \alpha_{LRW} x_{A_1})}{\sqrt{M_1}\sqrt{M_2 x_{A_1} + k_r}} \times \exp\left(-\frac{i}{2}\frac{(k_f \sin\psi - k_r)^2}{M_1}\right)\exp\left(\frac{ik_r}{2}\frac{M_2}{M_2 x_{A_1} + k_r}y_{A_1}^2\right). \tag{12}$$

In Eq. (12), $D = k_f a^2/2$ is the Rayleigh distance, $M_1 = \frac{ik_f B_n/D}{(1 + iB_n r_{10}/D)}\cos^2\psi$ and $M_2 = \frac{ik_f B_n/D}{(1 + iB_n r_{10}/D)}$.

2.4. Non-paraxial multi-Gaussian beam model of the LRW

It is not unexpected that the MGB model will lose accuracy as the paraxial approximation is used [11]. Here, the NMGB model is derived. Let the distance r_1 be expressed in terms of several approximate terms. A non-paraxial approximation is used to expand this distance to obtain a more accurate solution that is beyond the paraxial approximation [30]. In the case,

$$r_1 = \sqrt{(x - x_{s_0})^2 + (y - y_{s_0})^2 + z^2} \approx R_1 + \frac{(x_{s_0}^2 + y_{s_0}^2 - 2xx_{s_0} - 2yy_{s_0})}{2R_1}, \tag{13}$$

where $R_1 = \sqrt{x^2 + y^2 + z^2}$. Because the $1/r_1$ term is slowly varying in comparison with the $\exp(ik_f r_1)$ term in Eq. (6), $1/r_1$ can be replaced with $1/R_1$, and the pressure on the transducer surface is expressed as the superposition of Gaussian beams [18,19]. After some algebra, a non-paraxial multi-Gaussian beam expression for the pressure over the transducer face $p(x_{s_1}, y_{s_1}, \omega)$ can be obtained as

$$p(x_{s_1}, y_{s_1}, \omega) = \omega\rho_f\sum_{n=1}^{25} A_n\frac{\exp(ik_f R_1)}{(1 + iB_n R_1/D)} \times \exp\left(-\frac{ik_f}{2} \times \frac{1/R_1}{1 + iB_n R_1/D}x^2\right)\exp\left(-\frac{ik_f}{2} \times \frac{1/R_1}{1 + iB_n R_1/D}y^2\right). \tag{14}$$

The coordinates on the surface of the sample can be written as $(x = x_{s_1}\cos\psi,\ y = y_{s_1},\ z = r_{10} + x_{s_1}\sin\psi)$. r_{10} is the distance from the central point of (x_1, y_1, z_1) to that of (x_2, y_2, z_2) and here we treat it as the water path. Then R_1 can be expressed as

$$R_1 = \sqrt{(x_{s_1}\cos\psi)^2 + y_{s_1}^2 + (r_{10} + x_{s_1}\sin\psi)^2} \approx r_{10} + \frac{x_{s_1}^2 + y_{s_1}^2 + 2r_{10}x_{s_1}\sin\psi}{2r_{10}}. \tag{15}$$

Due to the fact that $1/R_1$ term is also a slowly varying function in comparison with the $\exp(ik_{p1}R_1)$ term in Eq. (6), we substitute $1/r_{10}$ with $1/R_1$ [18]. Then the velocity fields of the focused transducer $p(x_{s_1}, y_{s_1}, \omega)$ on S_1 area can be expressed as

$$p(x_{s_1}, y_{s_1}, \omega) = \omega\rho_f\sum_{n=1}^{25} A_n\frac{\exp(ik_f R_1)}{(1 + iB_n r_{10}/D)}\exp\left(\frac{i}{2}M_{11}x_{s_1}^2\right)\exp\left(\frac{i}{2}M_{22}y_{s_1}^2\right), \tag{16}$$

where $M_{11} = -k_f\frac{1/r_{10}}{1 + iB_n r_{10}/D}\cos^2\psi$ and $M_{22} = -k_f\frac{1/r_{10}}{1 + iB_n r_{10}/D}$. Then, using a non-paraxial approximation, the distance factor r_2 can be expressed as

$$r_2 = \sqrt{(x_{A_1} - x_{s_1})^2 + (y_{A_1} - y_{s_1})^2} \approx R_2 + \frac{y_{s_1}^2 - 2x_{A_1}x_{s_1} - 2y_{A_1}y_{s_1}}{2R_2}, \tag{17}$$

where $R_2 = \sqrt{x_{A_1}^2 + y_{A_1}^2}$. In addition, the Green's function of Eq. (4) can be simplified as

$$G(x_{A_1}, y_{A_1}, x_{s_1}, y_{s_1}) = \frac{\exp(ik_r r_2)}{\sqrt{r_2}} \approx \frac{1}{\sqrt{R_2}}\exp\left[ik_r\left(R_2 + \frac{y_{s_1}^2 - 2x_{A_1}x_{s_1} - 2y_{A_1}y_{s_1}}{2R_2}\right)\right]. \tag{18}$$

Placing Eqs. (14) and (18) into Eq. (3), the velocity field of the LRW $v(x_{A_1}, y_{A_1})$ can be reduced to

$$v(x_{A_1}, y_{A_1}) = \frac{T\omega\rho_f\pi}{2Q}\frac{\exp(i\pi/4)}{\sqrt{2\pi k_r}}\sum_{n=1}^{25}\frac{A_n\exp(ik_f r_{10} + ik_r R_2)}{\sqrt{M_{111}M_{222}R_2}(1 + iB_n r_{10}/D)} \times \exp\left(-\frac{i}{2}\frac{(k_f \sin\psi - k_r x_{A_1}/R_2)^2}{M_{111}}\right)\exp\left(-\frac{i}{2}\frac{(k_r y_{A_1}/R_2)^2}{M_{222}}\right), \tag{19}$$

where $M_{111} = k_f/r_{10} + M_{11}$ and $M_{222} = k_f/r_{10} + k_r/R_2 + M_{22}$. Finally, by including the attenuation of the LRW as it propagates, the NMGB model for the LRW velocity field can be expressed as

$$v(x_{A_1}, y_{A_1}) = \frac{T\omega\rho_f\pi}{2Q}\frac{\exp(i\pi/4)}{\sqrt{2\pi k_r}}\sum_{n=1}^{25}\frac{A_n\exp(ik_f r_{10} + ik_r R_2 - \alpha_f r_{10} - \alpha_{LRW} x_{A_1})}{\sqrt{M_{111}M_{222}R_2}(1 + iB_n r_{10}/D)} \times \exp\left(-\frac{i}{2}\frac{(k_f \sin\psi - k_r x_{A_1}/R_2)^2}{M_{111}}\right)\exp\left(-\frac{i}{2}\frac{(k_r y_{A_1}/R_2)^2}{M_{222}}\right). \tag{20}$$

Eq. (20) is one of the primary results of the article. From Eq. (20), it is observed that the velocity field mainly depends on the water path, parameters of the focused transducer, and attenuation of the LRW.

2.5. Numerical results

In this section, the LRW velocity field generated by a focused transducer are calculated using the RSI model, the NMGB model and the MGB model. For the calculations, several parameters are assumed, as shown in Table 1.

Fig. 2 shows the on-axis velocity fields calculated by the RSI model, the NMGB model and the MGB model. The off-axis velocity field components at $x = 25$, 39 and 66 mm for the three models are shown in Fig. 3. From these results, it is clear that the MGB method is not sufficiently accurate to determine the velocity field of the LRW, especially at the side lobes. Also, the velocity field of the off-axis calculated by the

Table 1
Parameters used for the calculations.

Incident angle ψ (°)	Velocity (m/s)				Transducer diameter D (mm)	Frequency f (MHz)	Focal length F (mm)	α_f (Np/m)	α_{LRW} (Np/m)
	c_f	c_p	c_s	c_r					
31	1480	6487	3139	2956	12.7	5	76	0.63	100

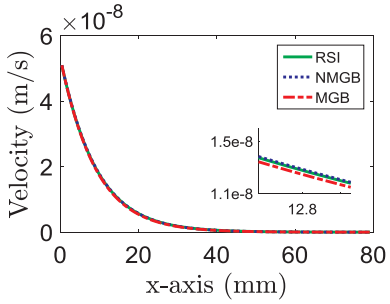

Fig. 2. The amplitude of on-axis velocity fields calculated by the RSI, the NMGB and the MGB models assuming a water path $r_{10} = 76$ mm.

methods of the NMGB model and the RSI model agree well with each other. The good agreement between these results confirms the accuracy of the NMGB model. More importantly, under the same parameters the calculation time for the RSI model, the NMGB model and the MGB model was 217.46 s, 0.31 s and 0.27 s on the same personal computer respectively, which demonstrated the obvious efficiency advantage of the NMGB model over the RSI model. This advantage is useful when the NMGB model is combined with other acoustic models, such as an ultrasonic measurement model and a diffuse backscatter model. Then we could use these acoustic models to evaluate the flaw size and the grain size near surface later. When we use these models to find the optimal evaluation value for the flaw size and the grain size, we generally need to fit the experimental data multiple times. In these cases, it is impractical to use the RSI model owing to excessive time cost.

3. Experiment

Experiments were conducted to check the derived results with respect to the propagation distance. Holes can be considered as standard reflectors. When the hole is small, the reflected velocity field from the hole can be considered as the velocity field of the LRW at the position of the hole. The velocity fields from the NMGB model will use for comparison with experiments in the section. The integral area should be infinite for obtaining the accurate velocity fields. However, the amplitude of velocity field outside S_1 area is small. Its influence on the LRW velocity filed calculation can be negligible. So, we choose the whole S_1 area for the integration. The main purpose of the experiment is to verify the validity of the NMGB model.

During each measurement, the longitudinal wave generated by the focused transducer is obliquely incident on the surface of the sample. Then the mode-converted LRW propagates along the water/solid surface and reflects from the hole. The reflected LRW converts into a longitudinal wave that is received by the transducer. Fig. 4 highlights the waveform transformation process. It is very complicated to simulate the whole process with a theoretical model. For the sake of simplicity, the reciprocity theory is introduced to solve the problem. The relationship between the wave radiated by the transducer and the echo reflected by the hole can be established by the reciprocity theory [11]. According to the reciprocity theory [11,31], the square of the LRW

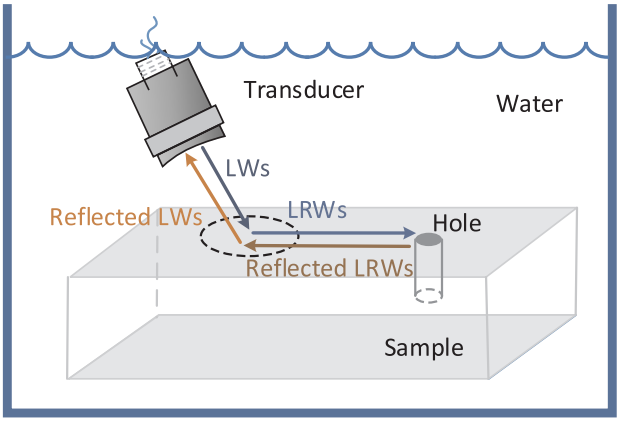

Fig. 4. Schematic showing the waveform transformation process of the LRW reflection from the hole.

velocity field at the holes can represent the reflected echo from the hole.

Holes with a diameter ϕ 2 mm and depth 20 mm were manufactured in a steel sample and an aluminum sample. The surface of each sample was sanded with 400 grit sandpaper, and polished to smoothness. An ultrasonic pulser/receiver (JSR DPR300) was employed to drive the immersion focused transducers in the experiment. Two transducers *Transducer A* (V309-SU-F3.00IN-PTF, Olympus) and *Transducer B* (V320-SU-F-3.00IN-PTF, Olympus) were used. The parameters of these two transducers are shown in Table 2. A high-speed data acquisition card AD link PCIE-9852 with sampling frequency of 200 MHz was employed to obtain the wave signals. A manipulator was used to control the distance between the transducer and the hole. The LRW was generated effectively when the incident angle was set to be 31° based on the Snell's law. The attenuation in water $\alpha_f = 0.63$ and 1.42 Np/m under 5 MHz and 7.5 MHz respectively, is calculated using the formula $\alpha_f = 25.3 \times 10^{-3} \times f^2$ in Ref. [11].

Fig. 5 shows the normalized amplitudes of the on-axis experimental results in steel, and those experimental results are compared with the NMGB model. Fig. 6 shows the comparisons for the case of aluminum. Fig. 7 shows the off-axis experimental results for steel and the model results. Fig. 8 shows the comparisons for the case of aluminum. A least squares method was used to determine the attenuation coefficients of the LRW α_{LRW} by fitting the experiment results with the NMGB model. Each experiment was repeated 10 times. When using *Transducer A* and *B* to do experiments, the fitting attenuation coefficients are $\alpha_{LRW} = 57$ and 82 Np/m, respectively for steel, and $\alpha_{LRW} = 165$ and 252 Np/m, respectively for aluminum. From these figures, experimental results agree well with the fitting NMGB model. The deviations between them may be caused by the noise of ultrasonic system, the roughness of the sample, the measurement errors induced by operators, and the system error which is mainly caused by the distortion of the returned Gaussian beam.

An incident Gaussian beam may not return a Gaussian shape (as the multi-Gaussian beam model assumes) as it propagates along the

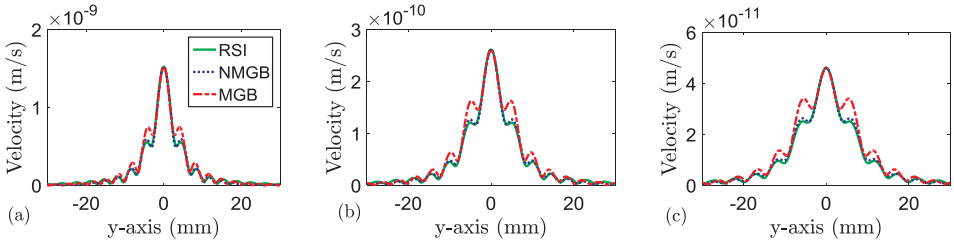

Fig. 3. The off-axis amplitude of velocity fields on the sample surface using the RSI, the NMGB, and the MGB models with $r_{10} = 76$ mm. (a) at $x = 25$ mm, (b) at $x = 39$ mm (c) at $x = 66$ mm. The amplitudes of these 3 positions are dramatically changed.

Table 2
Calibrated effective geometrical parameters for focused transducers.

Transducer	Central frequency (MHz)	Nominal parameter		Effective parameters	
		Diameter (mm)	Focal length (mm)	Diameter (mm)	Focal length (mm)
A	5	12.7	76	13.3	109
B	7.5	12.7	76	12.2	79.1

Note that the method to calibrate the parameters of focused transducers is shown in Ref. [32].

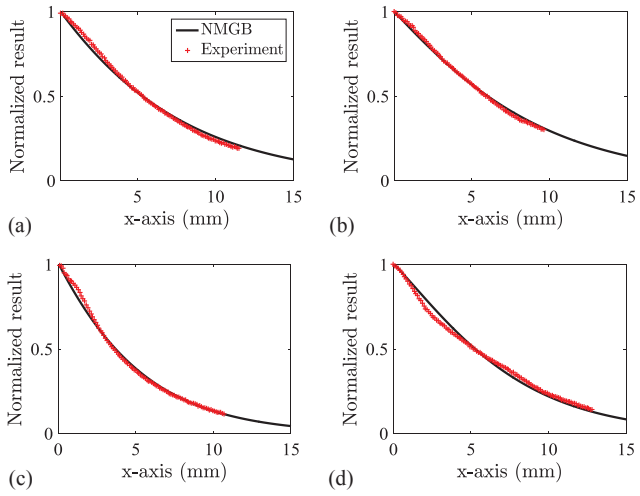

Fig. 5. Comparisons of the on-axis results from the steel sample at 5 MHz with α_{LRW} = 57 Np/m (a) water path r_{10} = 76 mm, (b) r_{10} = 66 mm, and 7.5 MHz with α_{LRW} = 82 Np/m (c) water path r_{10} = 76 mm, (d) r_{10} = 66 mm.

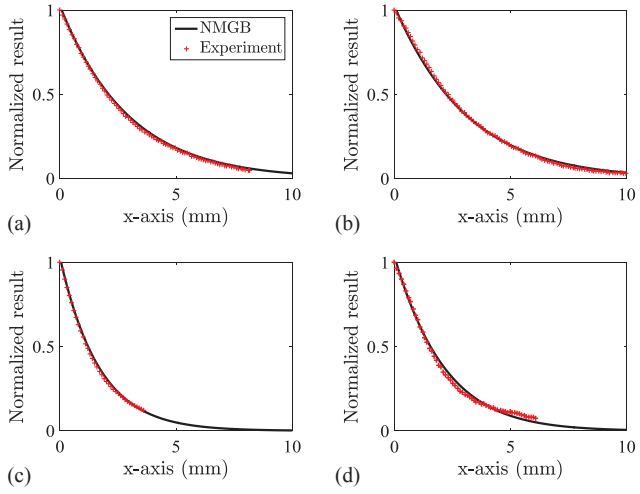

Fig. 6. Comparisons of the on-axis results from the aluminum sample at 5 MHz with α_{LRW} = 165 Np/m (a) water path r_{10} = 76 mm, (b) r_{10} = 66 mm, and 7.5 MHz with α_{LRW} = 252 Np/m (c) water path r_{10} = 76 mm, (d) r_{10} = 66 mm.

interface. Bertoni et al. [33] demonstrated that this distortion is controlled by a non-dimensional parameter, $h = \alpha_{LRW}\xi_0$, where ξ is the width of the incident beam, $\xi_0 = \xi/\cos\psi$, ψ is incidence angle and α_{LRW} is the attenuation coefficient of the LRW. They showed that for $h > 1$ this distortion is negligible and the reflected waves have a Gaussian profile like the incident waves; for $h < 1$ this distortion is not negligible and they observed a negative correlation between the non-dimensional parameter and distortion. When *Transducer B* is used, h for aluminum and steel are calculated as 1.84 and 1.19, respectively. For

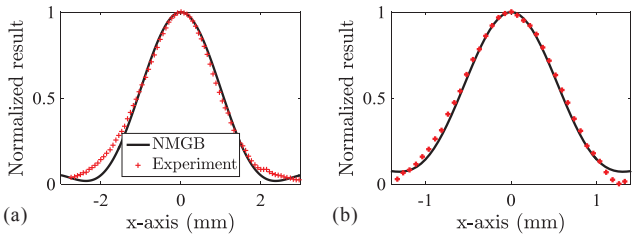

Fig. 7. Comparisons of the off-axis results from the steel sample at (a) 5 MHz with α_{LRW} = 57 Np/m and water path r_{10} = 76 mm and (b) 7.5 MHz with α_{LRW} = 82 Np/m and r_{10} = 76 mm.

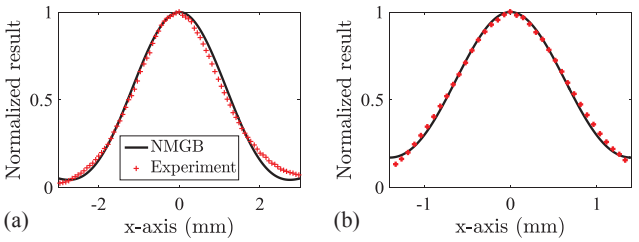

Fig. 8. Comparisons of the off-axis results from the aluminum sample at (a) 5 MHz with α_{LRW} = 165 Np/m and water path r_{10} = 76 mm and (b) 7.5 MHz with α_{LRW} = 252 Np/m and r_{10} = 76 mm.

Transducer A, h for the aluminum and steel are 0.60 and 0.42, respectively. The distortion for aluminum is smaller than that for steel, which agrees with the experimental results, for which the residual error of Fig. 4 is smaller than that of Fig. 3.

On the other hand, it should be noted in this work that the LRW attenuation coefficient for aluminum is larger than that for steel at the same frequency, which is different from common phenomena that the scattering level of aluminum should be lower at the same frequency because the degree of single-crystal anisotropy of aluminum is weaker [34]. The mean grain sizes of aluminum and steel samples measured by optical microscopy show there is only a small difference between them (measured as 49.4 ± 3.5 μm and 54.6 ± 2.8 μm). Therefore, the higher attenuation coefficient for aluminum is not thought to be caused by the grain size of the sample. One possible reason to explain the above-mentioned phenomenon is that there is leakage attenuation of the LRW. It is well known that the LRW attenuates quickly [4], so the component of leakage attenuation cannot be neglected, and it might even be the most dominant component. The acoustic impedance difference of water/aluminum interface is lower than that of water/steel, thus the LRW will leak more energy at the water/aluminum interface than at the water/steel interface.

The theoretical models for the attenuation induced by leakage have also been investigated preliminarily. For example, Schmerr et al. [13] proposed a model-based value to account for the leaky attenuations of the LRW when it propagates in the wedge and specimen interface. Based on this model, the values of the aluminum and steel at the frequency of 5 MHz can be calculated as 251.91 Np/m and 98.75 Np/m, respectively; the values of the aluminum and steel at the frequency of 7.5 MHz can be calculated as 377.87 Np/m and 148.13 Np/m, respectively. Thus, the values for the water/aluminum interface are larger than that for the water/steel interface. Note that the general trend of the model agrees with our experimental results; however, there are some overestimations in Schmerr's model. The reason still is not clear, and needs to be investigated in the future.

4. Conclusions

In this article, the LRW beams generated by immersion focused transducers are investigated theoretically and experimentally. The following conclusions can be drawn based on the analysis:

1. The new NMGB model method is an efficient approach to calculate the velocity fields of the LRW generated by the focused immersion transducer. Good agreement in the velocity fields using the RSI model and the NMGB model demonstrates the accuracy of the proposed model. Experiments also verified the accuracy of the NMGB model.
2. Experiments show that the velocity field can be significantly influenced by the water path and the frequency. In addition, it was shown that the attenuation of the LRW has a great influence on the velocity field.
3. The attenuation coefficient of the LRW can be estimated from experiments, because the component of diffraction attenuation can be eliminated by the NMGB model. The theoretical model for the leakage attenuation of the LRW will be studied in the future.

Acknowledgements

This paper was supported by the National Natural Science Foundation of China (Grant No. 51575541). The authors would like to express their gratitude to Drs. Shuzeng Zhang and Yongfeng Song for valuable discussions.

References

[1] W.P. Mason, Physical Acoustics: Principles and Methods, Academic Press, New York, 1964.
[2] J. Zhu, J.S. Popovics, F. Schubert, Leaky Rayleigh and Scholte waves at the fluid–solid interface subjected to transient point loading, J. Acoust. Soc. Am. 116 (2004) 2101–2110.
[3] O. Lefeuvre, P. Zinin, G.A.D. Briggs, Leaky surface waves propagating on a fast on slow system and the implications for material characterization, Ultrasonics 36 (1998) 229–232.
[4] G. Ghoshal, J.A. Turner, B.M. Wilson, Correlation of ultrasonic inspection of bearing components with bearing fatigue life, IEEE Joint Rail Conference, Williamstown, DE, 2008, pp. 165–170.
[5] P. Hu, J.A. Turner, C. Tarawneh, B. Wilson, A.J. Fuller, Multiple frequency ultrasonic detection of subsurface near-race inclusions for improved fatigue life performance, ASME, Joint Rail Conference, Mineta Transportat Inst, San Jose, CA, (2015) pp. V001T02A012.
[6] T. Xue, W. Lord, S. Udpa, Finite element simulation and visualization of leaky Rayleigh waves for ultrasonic NDE, IEEE Trans. Ultrason. Ferr. 44 (1997) 557–564.
[7] J.I. Kushibiki, N. Chubachi, Material characterization by line-focus-beam acoustic microscope, IEEE Trans. Sonics Ultrason. 32 (1985) 189–212.
[8] S.K. Nath, K. Balasubramaniam, C.V. Krishnamurthy, B.H. Narayana, Reliability assessment of manual ultrasonic time of flight diffraction (TOFD) inspection for complex geometry components, NDT & E Int. 43 (2010) 152–162.
[9] E. Kühnicke, Plane arrays–Fundamental investigations for correct steering by means of velocity field calculations, Wave Motion 44 (2007) 248–261.
[10] L. Koester, J.A. Turner, C. Zuhlke, D. Alexander, B. Wilson, C. Tarawneh, A.J. Fuller, Near-race ultrasonic inspection of tapered roller bearing components for non-metallic defects, ASME Rail Transportation Division Fall Technical Conference, Omaha, NE, 2012, pp. 107–110.
[11] L.W. Schmerr Jr., S.J. Song, Ultrasonic Nondestructive Evaluation Systems: Models and Measurements, Springer, New York, 2007.
[12] W. Li, Y. Cho, Combination of nonlinear ultrasonics and guided wave tomography for imaging the micro-defects, Ultrasonics 65 (2016) 87–95.
[13] L.W. Schmerr Jr, A. Sedov, Ultrasonic beam models for the generation of surface waves and plate waves with angle beam transducers, Review of Progress in QNDE, San Diego, CA, 2011, pp. 771–778.
[14] J.J. Wen, M.A. Breazeale, A diffraction beam field expressed as the superposition of Gaussian beams, J. Acoust. Soc. Am. 83 (1988) 1752–1756.
[15] D.S. Ding, Y. Zhang, J.Q. Liu, Some extensions of the Gaussian beam expansion: radiation fields of the rectangular and the elliptical transducer, J. Acoust. Soc. Am. 113 (2003) 3043–3048.
[16] H.J. Kim, L.W. Schmerr, A. Sedov, Generation of the basis sets for multi-Gaussian ultrasonic beam models – an overview, J. Acoust. Soc. Am. 119 (2006) 1971–1978.
[17] M. Spies, Modeling of transducer fields in inhomogeneous anisotropic materials using Gaussian beam superposition, NDT&E Int. 33 (2000) 155–162.
[18] X. Zhao, L.W. Schmerr Jr., A. Sedov, X. Li, Ultrasonic beam models for angle beam surface wave transducers, Res. Nondestruct. Eval. 27 (2016) 175–191.
[19] X. Zhao, L.W. Schmerr Jr., A. Sedov, X. Li, Simulation of ultrasonic surface waves with multi-Gaussian and point source beam models, AIP Conference Proceedings, 2014, pp. 556–562.
[20] T. Yanagita, T. Kundu, D. Placko, Ultrasonic field modeling by distributed point source method for different transducer boundary conditions, J. Acoust. Soc. Am. 126 (2009) 2331–2339.
[21] S. Banerjee, T. Kundu, D. Placko, Ultrasonic field modeling in multilayered fluid structures using the distributed point source method technique, J. Appl. Mech. 73 (2006) 598–609.
[22] S. Banerjee, T. Kundu, Semi-analytical modeling of ultrasonic fields in solids with internal anomalies immersed in a fluid, Wave Motion 45 (2008) 581–595.
[23] H. Jeong, L.W. Schmerr, Ultrasonic transducer fields modeled with a modular multi-Gaussian beam and application to a contact angle beam testing, Res. Nondestruct. Eval. 19 (2008) 87–103.
[24] J.R. Pettit, A.E. Walker, M.J.S. Lowe, Improved detection of rough defects for ultrasonic nondestructive evaluation inspections based on finite element modeling of elastic wave scattering, IEEE Trans. Ultrason. Ferroelectr. Freq. Control 62 (2015) 1797–1808.
[25] A. Sedov, L.W. Schmerr, S.J. Song, Ultrasonic scattering by a flat-bottom hole in immersion testing: an analytical model, J. Acoust. Soc. Am. 92 (1992) 478–486.
[26] I.A. Viktorov, Rayleigh and Lamb Waves: Physical Theory and application, Plenum Press, New York, 1967.
[27] J. Neuenschwander, T. Schmidt, T. Lüthi, M. Romer, Leaky Rayleigh wave investigation on mortar samples, Ultrasonics 45 (2006) 50–55.
[28] L.W. Schmerr Jr., Fundamentals of Ultrasonic Nondestructive Evaluation – A Modeling Approach, Springer, New York, 1998.
[29] S. Zhang, X. Li, H. Jeong, H. Hu, Modeling linear Rayleigh wave sound fields generated by angle beam wedge transducers, AIP Adv. 7 (2017) 15005.
[30] X. Zhao, T. Gang, Nonparaxial multi-Gaussian beam models and measurement models for phased array transducers, Ultrasonics 49 (2009) 126–130.
[31] T.P. Lerch, L.W. Schmerr, A. Sedov, Characterization of spherically focused transducers using an ultrasonic measurement model approach, Res. Nondestruct. Eval. 8 (1996) 1–21.
[32] S. Zhang, P. Hu, X. Li, H. Jeong, Calibration of focused circular transducers using a multi-Gaussian beam model, Appl. Acoust. 133 (2018) 182–185.
[33] H.L. Bertoni, T. Tamir, Unified theory of Rayleigh-angle phenomena for acoustic beams at liquid-solid interfaces, Appl. Phys. 2 (1973) 157–172.
[34] C.M. Kube, J.A. Turner, Ultrasonic attenuation in polycrystals using a self-consistent approach, Wave Motion 57 (2015) 182–193.